Journal of Building Engineering 22 (2019) 75–89

Contents lists available at ScienceDirect

Journal of Building Engineering

journal homepage: www.elsevier.com/locate/jobe

Experimental analysis for thermal storage performance of three types of plate encapsulated phase change materials in air heat exchangers for ventilation applications

T. Kumirai[a,*], J. Dirker[b,*], J. Meyer[b]

[a] CSIR Built Environment, PO Box 395, Pretoria 0001, South Africa
[b] Department of Mechanical and Aeronautical Engineering, University of Pretoria, Private bag X20, Hatfield, Pretoria 0028, South Africa

ARTICLE INFO

Keywords:
Phase change materials
Cooling power
Energy storage
Phase transformation duration

ABSTRACT

Due to climate change and rising global temperatures, energy demand associated with commercial and office building cooling, is projected to increase. Passive-cooling, based on phase change materials, can assist to moderate this increase, however relatively few modelling equations to describe its operating behaviour exists. In this experimental investigation the melting performance of three commercially available encapsulated phase change materials were evaluated for passive cooling applications in air ducts systems. Two paraffin type phase change materials and one salt hydrate phase change material with melting temperatures in the range of 22 °C and 28 °C were considered. Vertical orientated plate type encapsulations with a thickness of 10 mm and a pitch of 15 mm were tested for air inlet temperatures ranging from 30 °C to 35 °C and upstream air velocities ranging from 0.4 m/s and 0.9 m/s. The average effectiveness, cooling power, energy absorption, and phase transformation durations were determined. It was found that the average thermal effectiveness decreased with increased velocities and that the cooling power, which was inversely proportional to the phase transformation duration, increased with air flow rate and inlet air temperature. Based on the data a new empirical correlation model was developed which describes the cooling capacity of the in-duct phase change material plates.

1. Introduction

Of all the energy users, the built environment has been identified as having one of the largest untapped potential energy efficiency improvement opportunities which can greatly assist in the reduction of green-house gas emissions. It has been estimated that as much as 30–40% of the world's primary energy is consumed by the building sector [1]. The biggest use in this sector is space heating and cooling applications, which contribute to, at least, a third of greenhouse gas emissions [1]. This figure is expected to increase due to climate changes [2]. For example, the South African climate change model predicts that by mid-century the South African coast will warm by around 1–2 °C and the interior by around 2–3 °C. By 2100, warming is projected to reach around 3–4 °C along the coast, and 6–7 °C in the interior [3]. Such temperature increases will significantly increase the energy demand by building cooling applications. Thus, there is an urgent need to improve the energy efficiency in buildings and to reduce the peak heating and cooling loads.

The free cooling technique, which may assist in this regard, utilizes a thermal storage unit for accumulating cooling potential at night, and a mechanical system using fans and ducts to control and circulate air between the building exterior, the cooling potential storage unit and the interior of the building [1,4]. This type of cooling is favoured above nocturnal cooling (which uses the building structure to act as the thermal storage medium) because the accumulated cooling potential can be extracted during a controlled process when needed. Another drawback of nocturnal cooling is the challenge associated with achieving sufficiently high heat transfer coefficients to transfer heat between the building interior air and the building envelope [5]. Night ventilation is also less effective due to the lower thermal capacity available in the building envelope [6] as compared to thermal storage systems that utilize phase change material (PCM) type cooling potential accumulators. For this reason, air based heat exchange thermal storage devices that use PCMs have been studied experimentally, analytically and numerically. A brief outline of relevant studies in this regards is given below.

Alam et al. [7] compared the effectiveness of passive and free cooling application methods of PCMs when used as energy efficient

* Corresponding authors.
E-mail addresses: tkumirai@csir.co.za (T. Kumirai), Jaco.Dirker@up.ac.za (J. Dirker).

https://doi.org/10.1016/j.jobe.2018.11.016
Received 19 July 2018; Received in revised form 19 November 2018; Accepted 25 November 2018
Available online 28 November 2018
2352-7102/ © 2018 Elsevier Ltd. All rights reserved.

Nomenclature

A_s	Heat transfer surface area m^2
$A_{S,AE}$	Total surface area of steel duct between A to E m^2
$A_{N,AE}$	Total surface area of Neopor insulation between A to E m^2
B	Breadth of air duct m
$C_{p,air}$	Specific heat capacity of air J/kg K
$C_{p,dry\ air}$	specific heat capacity of dry air J/kg K
$C_{p,w}$	specific heat capacity of water vapour J/kg K
$C_{p,PCM,L/S}$	Specific heat capacity of the phase change material for both solid and liquid phases J/kg K
C_0, C_1, C_2, C_3, C_4	Correlation coefficients -
d_v	Absolute humidity kg/m^3
e_{PCM}	Thickness of aluminium encapsulation m
e_{Al}	Thickness of aluminium encapsulation m
e_s	Thickness of steel duct m
e_N	Thickness of Neopor insulation m
h_m	Latent heat of fusion per unit mass J/kg
h_c	Convective heat transfer coefficient W/m^2 K
H	Height of air duct m
k_{Al}	Thermal conductivity of aluminium W/m K
$k_{PCM,L/S}$	Thermal conductivity of the phase change material for both liquid and solid phases W/m K
k_s	Thermal conductivity of steel W/m K
k_N	Thermal conductivity of Neopor insulation W/m K
L_{AD}, L_{BD}, L_{CD}, L_{EG}, L_{AH}	Axial positions for components of the test section m
$\dot{m}_{air}$	Air mass flow rate kg/s
m_{PCM}	Mass of the phase change material kg
n_{mod}	Number of modules dimensionless
p	Pitch of phase change material plates m
P_i	Instantaneous power delivered to the heating element W
P	Barometric pressure Pa
P_w	Partial pressure of water vapour Pa
$\dot{Q}_{Loss,Air}$	Rate of energy lost (cooling rate) from air W
$\dot{Q}_{gain,ambient}$	Rate of energy lost to the surroundings W
$\dot{Q}_{gain,PCM}$	Rate of heat absorbed by the phase change material module W
$\dot{Q}_{heater}$	Instantaneous rate of heat transfer from the heating element to the air W
Q_{tot}	Energy absorbed by phase change material during the experiments J
$\dot{Q}_{obj}$	Desired maintained cooling power W
$\dot{Q}_i$	Cooling power delivered by the phase change material W
$R_{duct(\dot{m})}$	Duct thermal resistance K/W
$\bar{R}$	Average electrical resistance of heating element. Ω
R_{Al}	Thermal resistance of the aluminium encapsulate m^2K/W
R_N	Thermal resistance of Neopor insulation K/W
R_S	Thermal resistance of steel duct K/W
T_m	Phase change material melting temperature ˚C
$\bar{T}_i$	Average inlet air temperature ˚C
$\bar{T}_o$	Average outlet air temperature ˚C
$\bar{T}_{air}$	Mean bulk temperature ˚C
$\bar{T}_{air,AE}$	Mean bulk air temperature for duct section A-E. ˚C
$T_{air,Heater}$	Temperature of the air directly after the heater ˚C
T_a	Average room ambient air temperature ˚C
T_s	Plate surface temperature ˚C
$\bar{T}_{o,cor}$	Outlet air temperature corrected for heat losses ˚C
ΔT_{pcm}	Temperature difference between the air inlet temperature and the melting temperature. ˚C
Δt	Phase transformation duration s
V	Voltage V
W	Air humidity ratio kg/kg

Greek symbols

δ	Uncertainty indicator dimensionless
$\bar{\varepsilon}$	Effectiveness dimensionless
ρ_{PCM}	PCM density kg/m^3

retrofitting in a residential building for the summer climatic conditions of Melbourne (Australia). For passive application, PCM was installed in the ceilings of the house. In free cooling application, outdoor air was supplied to the indoor after passing it through a PCM storage unit. Validated simulation models were used to investigate the effectiveness of the two PCM application methods. Their results showed that the free cooling application was more effective than the passive application in terms of reducing the indoor air temperature. Free cooling application resulted in up to 1.8 ˚C reduction in indoor air temperature, compared to 0.5 ˚C for passive application.

Medved and Arkar [8] used an experimentally verified numerical model of a packed-bed PCM-air heat exchanger using cylinders installed in a ventilation air duct to study the efficiency in six European cities with different climatic conditions by determining cooling degree-hours for three summer months for each city. It was found that the PCM peak melting temperature should not differ by more than 2 ˚C from the ambient air temperature and that for the cases studied, the optimum size of the packed-bed unit should be between 1 kg and 1.5 kg of PCM per m^3/h of fresh ventilation air. Lazaro et al. [9] evaluated the thermal performance of two prototypes fitted with an organic PCM and an inorganic PCM respectively for a constant inlet air temperature. It was concluded that geometric parameters are of significant importance because the organic PCM exhibited shorter melting times and higher heat transfer rates, even though it had a lower thermal conductivity. Chaiyat and Kiatsiriroat [10] experimentally showed that the use of a packed bed paraffin wax PCM-air heat exchanger with spheres can improve the cooling efficiency of an air-conditioner and result in an energy cost saving. Halawa and Saman [11] found that for plate type storage modules, the temperature difference between the inlet air and the PCM melting temperature, the air gaps between plates, and plate thickness are critical parameters. Kabbara and Abdallah [12] experimentally found that Calcium Chloride Hydrate encapsulated in tubes exhibited higher heat fluxes and cumulative energy storage during melting at increased air flow rates and higher heat release rates during solidification at decreased air temperatures. Rajagopal and Velraj, [13] experimentally studied the cooling performance of paraffin encapsulated plates operated with circulated air from a room at different heat loads. It was found that the presence of the PCM storage module resulted in a significant ability to reduce the room temperature for significant periods of time. They suggested a possibility to design a modular heat exchanger with a proportional surface area to maintain thermal comfort within the room.

Even though it is clear that the presence of PCM-air based heat exchanger have advantageous energy usage implications, relatively few studies have focused on developing empirical mathematical characterisations of PCM thermal storage systems that are readily applicable to design. For instance, Castell et al. [14] used the effectiveness (ε)-NTU method and developed an empirical model which correlated the effectiveness and mass flux for a tube in a tank PCM storage system. Tay et *al.* [15] expanded on the research of Castell et al. [14] and validated the (ε)-NTU method. They carried out experiments for a one-tube-tank, two-tube-tank and four-tube- tank systems. They found that a single relationship existed for all the tested tube-tank systems which correlated effectiveness and mass flux of the tube-in-tank PCM storage system.

Even though some work has been done to evaluate the operation of

PCM passive cooling systems, there is still a lack of modelling equations which will enable a thermal HVAC engineer to correctly size and specify an in-duct PCM system. For that reason, the focus of this study is on providing new data and correlating it for a detailed ventilation air cooling thermal performance comparison between two types of paraffinic PCMs and a salt hydrate PCM that can be used in climatic conditions with summer ambient temperatures of 30–35 °C.

2. Experimental facility

Consider Fig. 1 that schematically gives the top view of the experimental test facility that consisted of a horizontal air duct setup which contained several components and sections that were connected in series and which was situated in a temperature controlled test room. Its purpose was to investigate the melting of different encapsulated PCMs for a defined initial state of the PCM, air flow rate and inlet air temperature. As will be described shortly, the setup was divided into an electrically inlet section (between A B), an upstream air passage (between B and F), the test section containing plate encapsulated PCM modules (between F and G), and a downstream air passage (between G and L).

2.1. Temperature controlled test room

The test room was located at the main campus of the Council for Scientific and Industrial Research in Pretoria (South Africa) at an elevation of 1386 m above sea level with an absolute barometric pressure of 87.8 kPa as obtained from an Oregon Scientific WMR300 indoor barometer with an accuracy of ± 100 Pa. The room temperature (T_a) was thermostatically controlled within 1 °C and maintained at preselected temperature values which ranged from 22 °C to 28 °C depending on the test requirements. Two calibrated T-type thermocouples connected to a data logger were used to monitor the air temperature that entered the heated inlet section. The thermocouples were located at two heights above the finished floor level sufficiently protected from direct influence and radiation of the heated inlet section. In order to define the thermodynamic state of the inlet air, the absolute air humidity was measured with an HOBO H8 logger which had an accuracy of ± 5% [16]. For the duration of the study the humidity was found to be between 5 g/m^3 and 10 g/m^3 which, depending on the air temperature, resulted in the relative humidity being between from 24% and 46%.

2.2. Heated inlet section and upstream air passage

The purpose of the inlet section and the upstream air passage was to receive air from the test room, heat the air to a prescribed temperature condition, allow for measurement of the bulk air temperature, and to pass the air to the test section.

The portion that contained the electrical resistance heater was circular while the main duct itself was rectangular. The inlet section had an inner diameter of 250 mm and a length of 330 mm (L_{AB} in Fig. 1). It was constructed from 3 mm galvanised steel sheeting. The heating element consisted of a Nickel Chromium alloy coil which had an element diameter of 10 mm. The spiralled outer diameter was 215 mm and the radial coil pitch was 20 mm. Its electric resistance was measured with an Agilent 34970A data logger to be 80 Ω ± 0.012 Ω at a coil surface temperature of 80 °C. The maximum specified power rating of the heater was 750 W and was powered by an adjustable transformer which received 230 V ± 5% at 50 Hz alternating current at its input. The output voltage of the transformer could be controlled to be between 0 V and 230 V, which was assumed to be sinusoidal. Both the heater resistance and the alternating current voltage output of the power supply was logged and monitored.

After the heating element, the flow passage transitioned from circular to a rectangular over an axial distance of 0.293 m (L_{BC}) to form a flow passage that had a breadth of 255 mm (B) horizontally and a height of 278 mm (H) vertically. The upstream passage had a length of 3.4 m (L_{CF}) and consisted of a number of rectangular duct sections which were connected by means of flanges and sealed with a silicon-based sealer to prevent air leakage.

As will be described later, the power input to the heater and the temperature difference of the air before and after the heater was used to determine the air mass flow rate. To reduce the effects of in-duct air temperature stratification after the heater due to buoyancy driven flow, passive free-rotating air mixing blades were inserted at point D (refer to Fig. 1) to disturb the thermal boundary layer and to enhance a uniform temperature distribution within the duct. The blades had an outer diameter of 250 mm and were placed at a distance L_{DF} of 1.6 m from the test section and conforms with the ASHRAE recommended mixing location [17].

The average bulk inlet air temperature ($\bar{T}_i$) to the tests section was obtained from five 0.8 mm diameter T-type thermocouples located at section E within the air-flow passage. They were positioned at a distance of 0.7 m (L_{EF}) before the test section. This flow distance was also based on the suggested ASHRAE recommendations [17]. One thermocouple was placed in the centre of the duct and the other four were each placed on the diagonals midway towards the duct corners. The thermocouple tips were held in position by taut strings (1 mm diameter) that were strung across the duct at the relevant positions. The use of five thermocouples reduced the uncertainty associated with the average inlet air temperature.

The entire upstream passage was thermally insulated from the test room by 100 mm thick Neopor™ insulation which was attached with adhesive to the external walls of the ducts and strapped tightly. The insulation had a density of 15 kg/m^3 and thermal conductivity of 0.032 W/mK (k_N). At worst case scenarios this resulted in a maximum heat loss of 3.6% of the heat added by the heating element.

2.3. Test section

Fig. 2 gives a schematic representation of the test section's (a) side view and (b) sectional view in the flow direction with gravity pointing downwards. It consisted of an acrylic glass shell containing fifteen

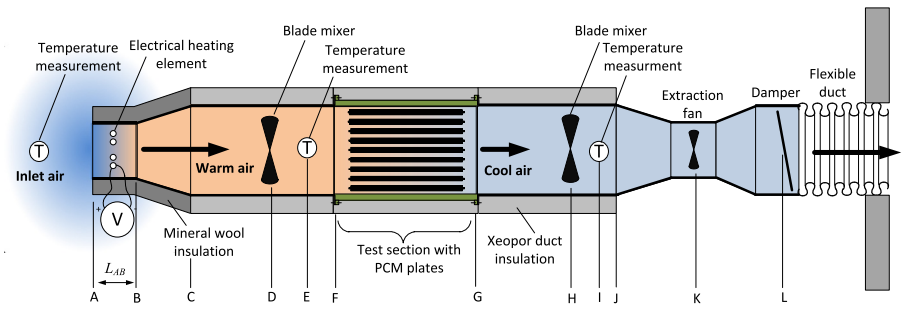

Fig. 1. Schematic diagram of the top view of the experimental setup (not drawn to scale).

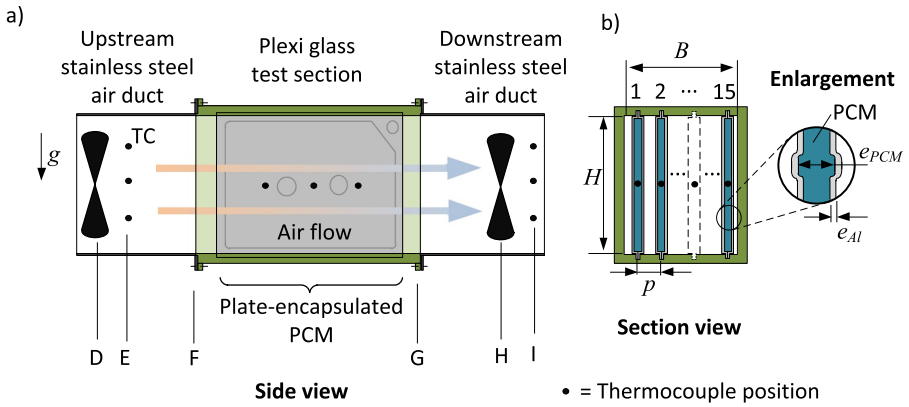

Fig. 2. Schematic side view representation of the test section containing the vertical plate-encapsulated PCMs (not drawn to scale).

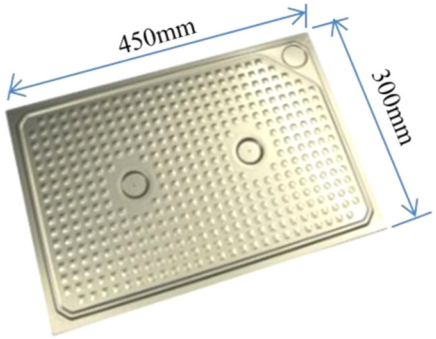

Fig. 3. Rubitherm™ plate encapsulated PCM.

vertically orientated commercial encapsulated PCM plates and was connected to the upstream and downstream air ducts by means of flanges using rubber gaskets. The internal cross section of the acrylic glass shell matched the internal cross section of the main duct (B x H) and had an axial length of 650 mm (L_{FG}). Its purpose was to enable the investigation of the effect of a PCM melting process by allowing the free passage of warm air over the PCM encapsulations and the ability to have the temperatures inside the PCM being monitored. To prevent significant heat loss or heat leakage to the test room, the external surfaces of the test section was also thermally insulated by Neopor™ insulation with a thickness of 100 mm.

The PCM encapsulations, obtained from Rubitherm™ Technologies and shown in Fig. 3, measured 300 mm high, 450 mm long and was at its thickest point 10 mm thick. Each plate consisted of a sealed aluminium shell patterned with bulges to enhance the exterior convective heat transfer coefficient. The shell had a thickness of e_{Al} = 1 mm [18] and the internal PCM had a thickness of up to e_{PCM} = 5 mm at the bulge locations (see Fig. 2b). The plates were installed vertically at a pitch of 15 mm (p) via slots in the upper and lower acrylic glass walls. The resultant gap size between adjacent plates was 5 mm, while the gap size at the two end walls on the side of the acrylic glass shell walls was 2.5 mm. A vertical orientation was selected to reduce the overall thermal resistance in the PCM plates by allowing solid PCM to settle at the bottom of the internal cavity during melting [19].

Characteristic PCM temperatures were monitored via internally installed T-type thermocouples within the interior of the plates as is indicated in Fig. 2b.

The selected PCMs had not yet been studied for Southern African climatic conditions and had melting temperatures ranging from 22 °C to 28 °C which correspond to the summer thermal comfort temperatures for South Africa's Gauteng province. This province accounts for 45% [22] of the country's office building sector based on lettable floor area and is located roughly at a latitude of 26.27°S, a longitude of 28.11°E, and an altitude of 1500 m.

The three PCMs (listed in Table 1) had similar values of latent heat of fusion (h_m) while the volumetric density of the salt hydrate was 1.71 times that of the paraffin waxes. This means that the mass of salt hydrate per plate was almost twice the mass of paraffin wax per plate. This indicates that the overall heat capacity of a plate containing the salt hydrates was approximately twice that of a plate containing paraffin wax. It should also be noted that the thermal conductivity (k_{CPM}) of the salt hydrate is three times higher that of paraffin waxes.

2.4. Downstream air passage

The downstream air passage (see Fig. 1) consisted of 2 duct sections, passive free-rotating air mixing blades, five T-type thermocouples, in-line tube fan and manual damper. Besides the fan motor controller, airflow through the system was also adjusted by a manual damper. The outlet damper had preselected operating positions which covered mass flows of approximately 0.03 kg/s to 0.06 kg/s which produced upstream duct air velocities of approximately 0.4–0.9 m/s.

The downstream duct was thermally insulated in the same fashion as the upstream duct.

The average outlet air temperature from the test section was always higher than ambient temperature during experimental tests. Because it was important to maintain a steady inlet air temperature to the test set-up, and to avoid test room ambient air temperature fluctuations, flexible ducting was used to exhaust outlet air from the test section to the outside of the test room.

2.5. Data acquisition system

An AgilentTM 34970A data logger switch unit with multiplexer cards was used for recording data from the test setup. This included 31 T-type thermocouples (ambient air, inlet and outlet air temperatures, and the PCM temperatures), the input voltage to the heating element, and the resistance across the heating element. Experimental measurements were logged at 5 s intervals and saved to a computer.

3. Experimental procedure

Before the main experiments were conducted, and before installation, the thermocouples were calibrated with a PD20R-30-A12E ANM Alliance water bath unit which was equipped with a performance digital temperature controller which was capable of maintaining a temperature stability of ± 0.005 °C in the water body.

The main work of this study consisted of a series of melting experiments at specific air inlet temperatures and air mass flow rates. Table 2 supplies a summary of the test matrix for a particular PCM

Table 1
Thermophysical properties of RT25, RT27 and SP24E [20].

PCM	T_m (°C)	h_m (kJ/kg)	$C_{p,PCM,L/S}$ (kJ/kgK)	$k_{PCM,L/S}$ (W/mK)	ρ_{ss} (kg/m^3)	ρ_{ls} (kg/m^3)	m_{pcm} (kg)
RT25	22–26	170	2	0.2	880	760	0.58
RT27	25–28	180	2	0.2	880	760	0.58
SP24E	24–25	180	2	0.6	1500	1400	1

Table 2
Melting experiments matrix for each PCM type.

Experiment	Approximate inlet air temperature (°C) ± (0.8) °C	Approximate duct air velocity (m/s) ± (0.05) m/s
1	30	0.4
2	32	0.4
3	35	0.4
4	30	0.7
5	32	0.7
6	35	0.7
7	30	0.9
8	32	0.9
9	35	0.9

covering inlet air temperatures of approximately 30, 32 and 35 °C and duct air velocities covering approximately 0.4 m/s, 0.7 m/s and 0.9 m/s. This resulted in 27 experiment types in total for the three PCMs under consideration.

Before each experiment, it was important to ensure that the PCM in each plate was at a uniform preselected solid state, well below its melting temperature. This was done by setting the air temperature in the test room to 19 °C and circulating the cold room air through the test sections for prolonged periods of time until uniform temperatures were achieved across the plates. Normally PCM temperatures around 19.5–20.5 °C were achieved after 9 h. The experiment was left to run until the cooling potential of the PCM plates were significantly depleted indicted by when the down-steam outlet air temperature (after the test section) was within 0.5 °C of the upstream inlet air temperature.

4. Data reduction and uncertainty analysis

4.1. Air mass flow rate

The air flow rate at time t through the test section was determined by applying an energy balance for the air passing over the inlet electrical heating element. It was assumed that there is negligible heat loss through the insulation around the heating section due to its relatively shorter length, so that the instantaneous rate of heat transfer to the air at the heater ($\dot{Q}_{heater}$) was equated to the instantaneous electric power input to the heating element (P_i).

$$\dot{Q}_{heater} = P_i = \frac{V^2}{\bar{R}} \tag{1}$$

The electric voltage (V) and the instantaneous electric resistance ($\bar{R}$) was measured over the heating element terminals by the data logger.

The air mass flow rate was expressed via the energy equation as follows in terms of the heat transfer from the heater and the heat loss ($\dot{Q}_{loss,AE}$) in the air duct between points A and E:

$$\dot{m}_{air} = \frac{\dot{Q}_{heater} - \dot{Q}_{loss,AE}}{C_{p,air}(\bar{T}_i - \bar{T}_a)} \tag{2}$$

The air temperature at the inlet before the heater ($\bar{T}_a$) was obtained from the arithmetic average of the two thermocouples that were installed before the inlet section, the downstream air temperature after the heater ($\bar{T}_i$) was obtained from the arithmetic average of the five thermocouples that were installed in the air duct at position E in Fig. 1 and 2, and the specific heat capacity of the air ($C_{p,air}$) was calculated as follows in terms of the specific heat capacities of the dry air component and the water vapour component:

$$C_{p,air} = C_{p,\ \ dry\ air} + WC_{p,w} \tag{3}$$

A value of 1.005 kJ/kg K [23] was adopted for the dry air specific heat capacity ($C_{p,dry\ air}$) which is suitable for the air temperature range of interest to this study and which has been found to remain approximately constant for a temperature range of 20–40 °C. For the specific heat capacity of the water vapour ($C_{p,w}$) a value of 1.82 kJ/kgK was adopted [24]. The absolute humidity (W) was calculated as follows [25]:

$$W = 0.62198\frac{P_w}{P - P_w} \tag{4}$$

The partial water vapour pressure (P_w) can be expressed as follows [26]:

$$P_w = 461.9\bar{T}_a \times d_v \tag{5}$$

The absolute humidity ratio (d_v) was obtained from the HOBO humidity sensor.

In Eq. (2) the heat loss from the duct was calculated as follows:

$$\dot{Q}_{loss,AE} = \frac{\bar{T}_{air,AE} - \bar{T}_a}{R_S + R_N} \tag{6}$$

The mean bulk air temperature between sections A and E was calculated as follows:

$$\bar{T}_{air,AE} = \frac{T_{air,\ \ Heater} + \bar{T}_i}{2} \tag{7}$$

Steel duct thermal resistance between sections A and E was calculated as follows:

$$R_S = \frac{e_s}{k_s A_{S,AE}} \tag{8}$$

Neopor thermal insulation thermal resistance between sections A and E was calculated as follows:

$$R_N = \frac{e_N}{k_N A_{N,AE}} \tag{9}$$

Here areas A_S and A_N where based on length AE of 2.7 m.

The value of R_S was five orders of magnitude less than R_N therefore it was ignored.

$$\dot{Q}_{loss,AE} = \frac{\bar{T}_{air,AE} - \bar{T}_a}{R_N} \tag{10}$$

Eqs. (2, 7 and 10) were solved iteratively to calculate the heat loss ($\dot{Q}_{loss,AE}$) and air mass flow rate ($\dot{m}_{air}$).

4.2. Instantaneous cooling power

The instantaneous cooling power ($\dot{Q}_i$ or $\dot{Q}_{gain,PCM}$) delivered by the test section (PCM plates) was evaluated by applying energy balance around the air in section E to I (See the schematic diagram Fig. 1):

$$\dot{Q}_{Loss,Air} = \dot{Q}_{gain,PCM} + \dot{Q}_{gain,ambient} \tag{11}$$

In this equation the total heat loss from the air stream in the test section is attributed to the combined heat transfer to the PCM as well as the heat transfer to the ambient air around the test duct.

The total heat transfer rate from the air can be expressed in terms of the change of air enthalpy across the PCM test section by making use of the specific heat capacity of the air:

$$\dot{Q}_{Loss,Air} = \dot{m}_{air} C_{p,air}(\bar{T}_i - \bar{T}_o) \tag{12}$$

The outlet air temperature, measured at point I, was determined by taking the arithmetic average of the 5 thermocouples at that location.

The heat rate gain into the PCM can also be expressed in terms of the change of the enthalpy of the PCM, however, because phase change occurs, the use of specific heat is not suitable. For demonstration purposes the process is assumed for a brief moment to occur fully within the phase transition period (Δt) which allows the enthalpy change to be expressed in terms of the latent heat of fusion:

$$\dot{Q}_{gain,PCM} = m_{PCM}\frac{\Delta h_m}{\Delta t} \tag{13}$$

The heat transfer rate to the ambient air around the test duct can be expressed in terms of the relative temperature difference between the air flow in the test duct and the air outside the test duct, and the thermal resistance of the test duct wall:

$$\dot{Q}_{gain,ambient} = \frac{\bar{T}_{air} - T_a}{R_{duct(\dot{m})}} \tag{14}$$

It should be noted that the thermal resistance of the duct wall was dependent on the inner convective heat transfer coefficient on the inside of the test duct, the effective conductive resistance of the duct wall layers (including the thermal insulation around the duct), and the outer convective heat transfer coefficient on the outside of the insulation layer. Because the inner convective heat transfer coefficient was dependent on the mass flow rate of the air inside the test duct, which explains the dependence of R_{duct} on $\dot{m}$.

By substituting Eqs. (12)–(14) into Eq. (11), the instantaneous heat absorption into the PCM can be expressed as:

$$\dot{Q}_i = \dot{Q}_{gain,PCM} = m_{PCM}\frac{\Delta h_m}{\Delta t} = \dot{m}_{air}C_{p,air}(\bar{T}_i - \bar{T}_o) - \frac{\bar{T}_{air} - T_a}{R_{duct(\dot{m})}} \tag{15}$$

To determine $R_{duct(\dot{m})}$, the experiment was run without the PCM plates placed in the test section. Heated air was passed through the test duct and the temperatures before and after the test section was measured. Any steady state temperature decrease over the test section was thus due to only the heat loss from the internal air through the duct wall. Thus, with the absence of PCM mass in Eq. (15) ($m_{PCM} = 0$), the thermal resistance can be expressed in terms of the specific heat of the air, the inlet air temperature, the outlet air temperature, the ambient air temperature and the air mass flow rate:

$$R_{duct(\dot{m})} = \frac{\frac{1}{2}(\bar{T}_i + \bar{T}_o) - T_a}{\dot{m}_{air}C_{p,air}(\bar{T}_i - \bar{T}_o)} \tag{16}$$

Note, as mentioned earlier $R_{duct(\dot{m})}$ is a function of the air mass flow rate (i.e. the higher the air mass flow rate, the lower the $R_{duct(\dot{m})}$ value) Therefore, to determine whether or not $\dot{Q}_{gain,ambient}$ contributed significantly in the energy balance (Eq. (7)), the $R_{duct(\dot{m})}$ value for the highest tested air mass flow rate was evaluated. The calculated average $R_{duct(\dot{m})}$ (2.78 K/W) was then used to evaluate $\dot{Q}_{gain,ambient}$ for the experimental tests which had air mass flow rate of 0.06 kg/s. A range ($\%\frac{\dot{Q}_{gain,ambient}}{\dot{Q}_{gain,PCM}}$) of 0.2–9.4% was calculated for the entire experimental duration. For the phase transformation period, the range ($\%\frac{\dot{Q}_{gain,ambient}}{\dot{Q}_{gain,PCM}}$) was 0.51–0.98%. These contributions were considered significant and therefore were taken into account in calculating of $\dot{Q}_{gain,PCM}$.

For the calculation of instantaneous cooling power delivered by a PCM module ($\dot{Q}_i = \dot{Q}_{gain,PCM}$) for different operating conditions of air temperature and air mass flow rate, the following equation was applied on the experimental data.

$$\dot{Q}_i = \dot{m}_{air}C_{p,air}(\bar{T}_i - \bar{T}_o) - \frac{\bar{T}_{air} - T_a}{R_{duct(\dot{m})}} \tag{17}$$

Here $R_{duct(\dot{m})}$ was regarded to be a constant value of 2.78 K/W calculated as explained above.

4.3. Determination of phase transformation duration

The phase transformation period was the time interval during which the PCM changed from solid to liquid phase. During the same period both latent and sensible heat storage mechanisms were active. However, the latent heat storage component was the dominant mode of heat storage.

Values of the melting temperature ranges of the PCMs were supplied by the PCM supplier (see Table 1). The thermocouples that were installed at specific points within the PCM indicated the PCM temperatures during the heat absorption period. As mentioned earlier, a total of 18 thermocouples were placed at various points in the PCM plates to establish the PCM average temperature. The phase transformation period was defined as the time lapse between the moments when the average PCM temperature reached the manufacturer supplied solidus and liquidus temperatures. An example of a graph showing the PCM temperatures versus time is given in Fig. 4.

It was possible to determine the phase transition periods from the supplied temperature properties for the paraffin type PCMs (RT25 and RT27), but not for the salt-hydrate PCM (SP24E) because it was not clear from the manufacturer data if definite liquidus and solidus temperatures existed for this material type. Therefore, phase transformation periods are reported for the RT25 and RT27 only.

4.4. Effectiveness

The effectiveness of each PCM-module ($\bar{\varepsilon}_m$) was defined as the ratio of actual energy absorbed during phase transformation to the maximum possible energy that can be absorbed or released by the air. The effectiveness calculation is valid for the phase transformation period only. Eq. (18) was used to calculate the average effectiveness for the duration of phase transformation for the RT25 and RT27 modules. The average effectiveness of the SP24E module was not determined because SP24E did not melt but rather went through continuous dehydration reactions over a temperature range that was wider than that specified by the PCM supplier.

$$\bar{\varepsilon}_m = \frac{\bar{T}_i - \bar{T}_o}{\bar{T}_i - \bar{T}_m} \tag{18}$$

Because there was an energy loss to the ambient through the air duct wall, the experimentally measured outlet temperature did not reflect the true cooling potential of the PCM plates. In order to determine

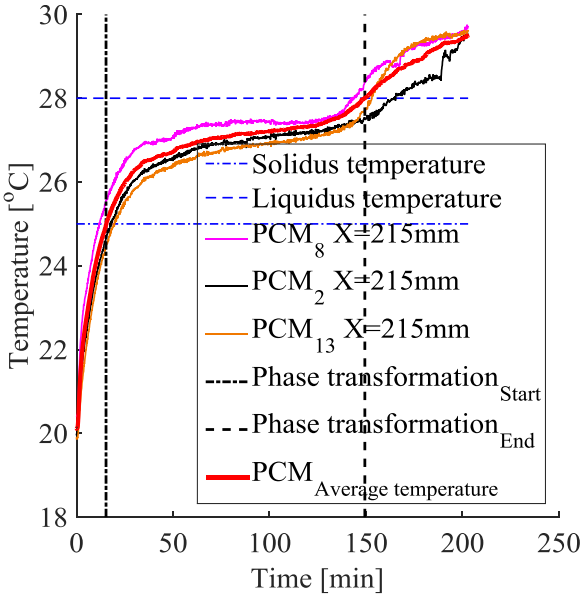

Fig. 4. Illustration for the determination of phase transformation duration.

the cooling potential of the PCM plates if they were operational in an adiabatic air duct, the heat loss as calculated in Eq. (14) (0.2–9.4% of the $\dot{Q}_{gain,PCM}$ over the entire experimental duration and from 0.51–0.98% during the PCM phase transformation period), was taken into consideration to determine the hypothetical adiabatic air duct exit air temperature as follows:

$$\bar{T}_{o,cor} = \bar{T}_i - \left(1 - \%\frac{\dot{Q}_{gain,ambient}}{\dot{Q}_{gain,PCM}}\right)(\bar{T}_i - \bar{T}_o) \quad (19)$$

4.5. Energy absorbed

The amount of total energy absorbed by the PCM modules for the whole duration of the experiment was calculated by integrating the instantaneous heat rate with time for the whole experimental duration:

$$Q_{tot} = \int_{t=0}^{t=Final} \dot{Q}_i dt \quad (20)$$

4.6. Uncertainty analysis

Experimental results must be accompanied with the relevant uncertainties (δ) [27]. Table 3 gives the experimental equipment uncertainties. The uncertainties of the specific heat capacity, the inlet and outlet air temperatures, as well as the air temperature difference, mass flow rate and instantaneous heat transfer rate were calculated using the uncertainty propagation method of Kline and McClintock's [28] and given in Table 4.

The uncertainty for the instantaneous heat transfer rate for the SP24E module is higher than that for RT25 because the uncertainties for RT25 module are averaged for the phase transformation duration only. The temperature difference between the air inlet temperature ($\bar{T}_i$) and the air outlet temperature ($\bar{T}_o$) tended to zero towards the end of the experiment; therefore the higher uncertainties in the thermocouple measurements lead to higher uncertainty in the calculation of cooling power when considering the entire experimental duration for SP24E module. As expected, the cooling power tended to zero towards the end of the experiment as the temperature of PCM approached the inlet air temperature.

5. Results and discussion

5.1. PCM temperature distribution during melting

Figs. 5 and 6 give time plots of the inlet air temperature ($\bar{T}_i$), the outlet air temperature ($\bar{T}_o$) All of the figures are for an intended inlet air temperature of 30 °C and a mass flow rate of 0.03 kg/s. Fig. 5 is for RT27, Fig. 6 is for RT25 and Fig. 7 is for SP24E.

For all two cases the average outlet air temperature ($\bar{T}_o$) was lower than the average inlet air temperature ($\bar{T}_i$). This trend was observed for all other air mass flow rates and inlet air temperatures for all the three PCM types. This indicates the air cooling behaviour of the PCM plates during heat absorption (predominately melting) into the PCM. For all the cases there was a higher temperature difference between $\bar{T}_i$ and $\bar{T}_o$ at the start of the experiments. This can be attributed to the higher temperature difference between the inlet air temperature (approximately 30 °C) and the initial PCM temperature (20 °C). The higher initial temperature differences caused initially higher heat transfer rates between the air and the PCM.

Table 3
Experimental equipment uncertainties.

	Uncertainty
Thermocouple	± 0.1 °C
Oregon Scientific WMR300 indoor barometer	± 0.1 kPa
Agilent 34970A data logger voltage measurement	± 0.1 V
Agilent 34970A data logger electrical resistance measurement	± 0.012 Ω
Humidity	± 5%

The profiles of the PCM temperature against time for the SP24E (salt hydrate) modules are different when compared to those of the RT27 (paraffin) modules. The profiles for SP24E were found to be almost linear and that of RT27 are asymptotic for a lower temperature difference between inlet air temperature and PCM melting temperature (ΔT_{pcm}) until fully molten. For higher ΔT_{pcm} the profiles for RT27 (paraffin) become sigmoidal (S-curved). The difference in the profiles is due to the different mechanisms by which heat is absorbed. For SP24E (salt hydrate) the heat is absorbed for dehydration reactions; the linear profile suggests that the dehydration reactions are continuous.

The melting temperature range of SP24E specified by the manufacturer suggests a very short melting period for the salt hydrate (range of 25–285 s) but the experimental data suggested otherwise. The SP24E is not a single salt hydrate but rather a mixture of salt hydrates (40–60% $CaCl_2$, 1–20% KCl, 0–5% NaCl, 1–20% NH_4Cl and 0–5% $MgCl_2$ [21]). This explains the absence of a single well defined melting temperature. The SP24E PCM temperature-time profile in Fig. 6 do not show the incidences of start and completion of the dehydration process hence making it difficult to estimate an accurate phase transformation duration. The determination of an accurate melting temperature range for SP24E falls outside of the scope of this work.

The PCM temperatures of the plates directly next to the side walls of the air duct (PCM_2 and PCM_{13}) were lower than middle plate PCM temperature (PCM_8). This can be attributed to the velocity boundary layer effect. The inlet air velocity towards the end plates is expected to be lower than the middle plates therefore lower heat transfer rates between air and PCM at the end plates when compared to middle plates.

5.2. PCM melt front

PCM temperature distribution in plate 8 (the centre-most plate) is shown in Fig. 7 for RT27 PCM for an air mass flow rate of 0.03 kg/s and inlet air temperature of 32 °C. As mentioned earlier, three PCM temperatures were measured at the following axial distance from the leading edge: 145 mm (PCM_{16}: upstream side), 215 mm (PCM_{17}: middle of plate) and 315 mm (PCM_{18}: downstream side).

For all cases a general trend was observed that the upstream PCM temperature (PCM_{16}) was always greater than the middle (PCM_{17}) and downstream (PCM_{18}) PCM temperatures. The downstream PCM temperature was observed to be the lowest of the three PCM temperatures. This trend was repeated for other air mass flow rates and inlet air temperatures for all the three PCM types. This shows that for thin PCM encapsulations for ventilation applications, the PCM melting front moves from the leading edge to the trailing edge.

5.3. RT27 AND RT25 phase transformation time, effectiveness, and average cooling power

Tables 5 and 6, show the air mass flow rates through the PCM modules, the average inlet air temperatures for the duration of the phase transformation, time average outlet air temperatures for the duration of the phase transformation, phase transformation times, calculated average effectiveness and calculated average air cooling power for the duration of the phase transformation.

5.4. Effectiveness analysis: effect of air mass flow rate and inlet air temperature on average effectiveness

Eq. (18) was used to calculate average effectiveness. The equation applies only for the phase transformation duration. The calculation of phase transformation time for the paraffinic PCMs (RT27 and RT25) was determined by the use of the average PCM temperature-time profile

Table 4
Calculated uncertainties considering phase transformation duration for RT25 module and whole experimental duration for SP24E.

$\dot{m}_{air}$ (kg/s)	$\bar{T}_i$ (°C)	$\delta C_{p,air}$ (kJ/kg K)	$\delta \bar{T}_i$ (°C)	$\delta \bar{T}_o$ (°C)	$\delta \Delta T_{i,o}$ (°C)	$\delta \dot{m}_{air}$ (kg/s)	$\delta \bar{Q}_i$ (%) for RT25	$\delta \bar{Q}_i$ (%) for SP24E
0.03	30	6.55E−05	0.045	0.045	0.063	0.0010	10.15	24.17
0.03	32	6.53E−05	0.045	0.045	0.063	0.0015	6.8	33.68
0.03	35	6.557E−05	0.045	0.045	0.063	0.0014	5.31	16.51
0.05	30	6.611E−05	0.045	0.045	0.063	0.0012	7.83	19.55
0.05	32	6.62E−05	0.045	0.045	0.063	0.0015	6.88	18.78
0.05	35	6.599E−05	0.045	0.045	0.063	0.0019	4.75	23.06
0.06	30	6.565E−05	0.045	0.045	0.063	0.0017	9.05	22.15
0.06	32	6.559E−05	0.045	0.045	0.063	0.0020	7.49	25.28
0.06	35	6.567E−05	0.045	0.045	0.063	0.0020	5.73	19.06

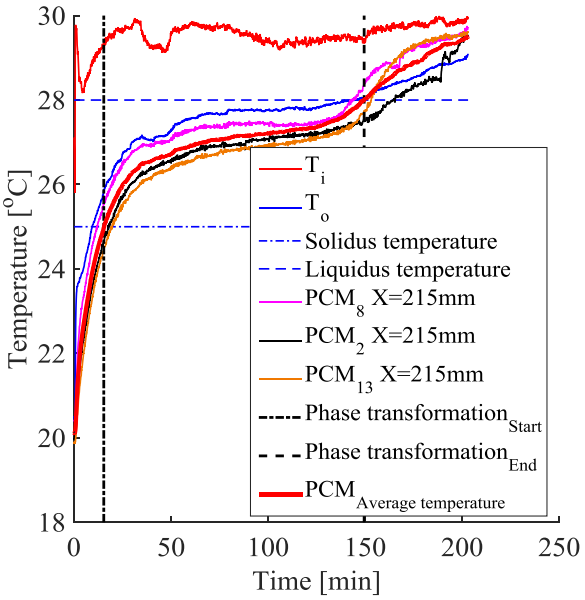

Fig. 5. Logged temperatures for the RT27 module for an intended inlet air temperature of 30 °C and an airflow rate of 0.03 kg/s.

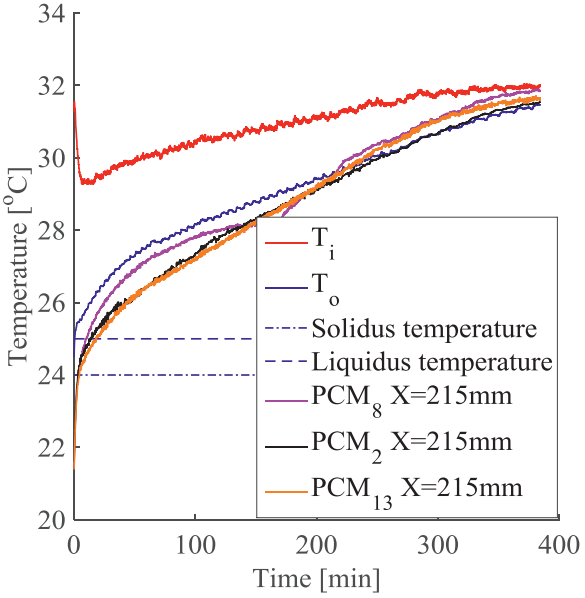

Fig. 6. Logged temperatures for the SP24E module for an intended inlet air temperature of 30 °C and an airflow rate of 0.03 kg/s.

as explained above. The averages of the melting temperature ranges for the paraffins (RT27 and RT25) were used to represent the peak melting temperature for the paraffins and were regarded as the PCM melting

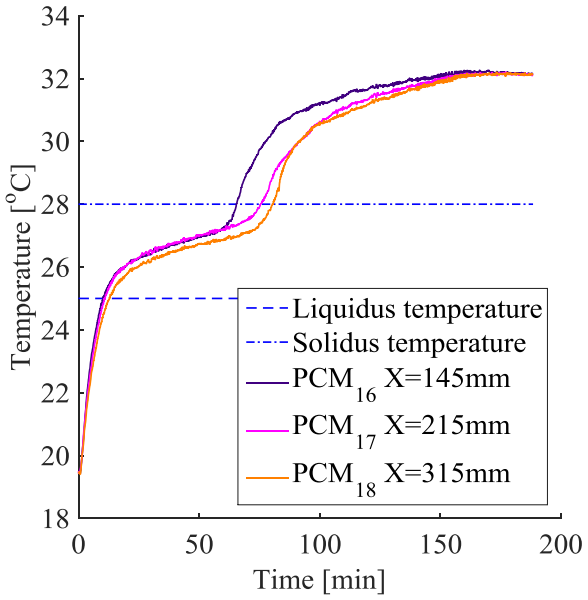

Fig. 7. PCM temperature distributions for RT27 in the centre plate measured at three axial locations for an air mass flow rate of 0.03 kg/s and an inlet air temperature of 32 °C.

Table 5
Experimental parameters and results for RT25 considering the phase transformation period only.

Module type	$\dot{m}_{air}$ (kg/s)	$\bar{T}_i$ (°C)	$\bar{T}_o$ (°C)	Phase transformation time (s)	$\bar{\varepsilon}$	$\dot{Q}_{ave}$(W)
RT25	0.03	29.8	26.3	2315	0.60	118
	0.03	31.7	27.1	1515	0.59	202
	0.03	34.5	28	1215	0.62	239
	0.05	30.9	27.1	1520	0.56	186
	0.05	31.4	27.4	1215	0.54	228
	0.05	34.6	28.5	845	0.57	285
	0.06	29.2	26.4	1560	0.55	188
	0.06	31.4	27.3	1030	0.55	258
	0.06	32.8	28	570	0.54	327

temperatures ($\bar{T}_m$) in Eq. (18).

The data from Tables 5 and 6 were used to plot the effect of air mass flow rate and air inlet temperature on average effectiveness for the RT25 and RT27 modules as are shown in Figs. 8 and 9.

From Figs. 8 and 9, the effect of air mass flow rate on the effectiveness can be interpreted considering a fixed average inlet air temperature ($\bar{T}_i$). Both Figures show that the average effectiveness of the PCM modules decreases with increasing convective air mass flow rate as expected. Low air mass flow rate ensure longer warm air residence time. For the RT27 module, at a 30 °C inlet air temperature, the average effectiveness was 0.66 for an air mass flow rate of 0.03 kg/s and 0.56

Table 6
Experimental parameters and results for RT27 considering the phase transformation period only.

Module type	$\dot{m}_{air}$ (kg/s)	$\bar{T}_i$ (°C)	$\bar{T}_o$ (°C)	Phase transformation time (s)	$\bar{\varepsilon}$	$\dot{Q}_{ave}$ (W)
RT27	0.03	29.5	27.5	8050	0.66	60
	0.03	31.6	28.3	3785	0.65	118
	0.03	34.6	29.4	1965	0.65	154
	0.05	29.7	27.7	3670	0.62	104
	0.05	31.8	28.8	2220	0.56	154
	0.05	34.7	30.1	1375	0.56	223
	0.06	30.4	28.2	2930	0.56	126
	0.06	31.9	28.9	1870	0.55	175
	0.06	34.7	30.4	1155	0.52	254

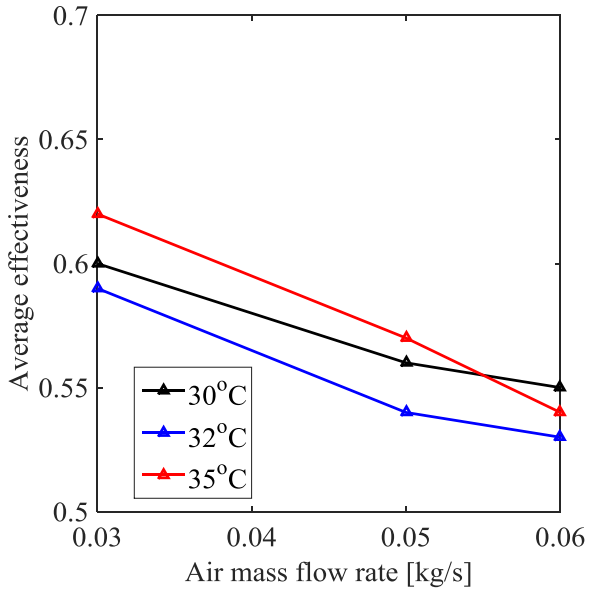

Fig. 8. Effect of air mass flow rate and air inlet temperature on the average effectiveness of the RT25 module.

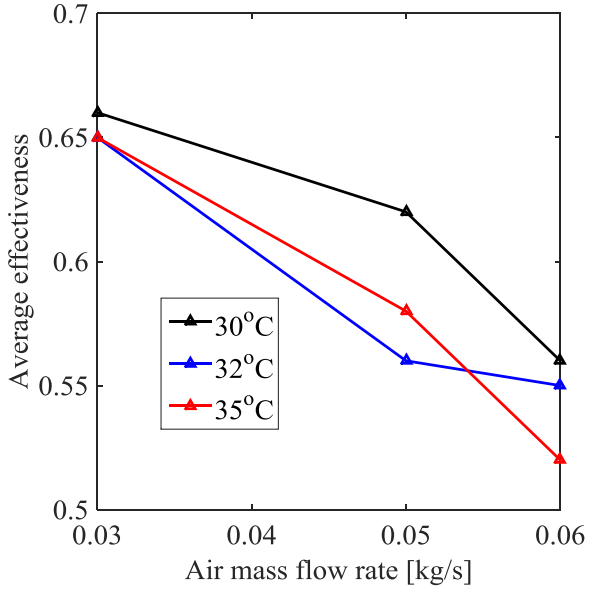

Fig. 9. Effect of air mass flow rate and air inlet temperature on the average effectiveness of the RT27 module.

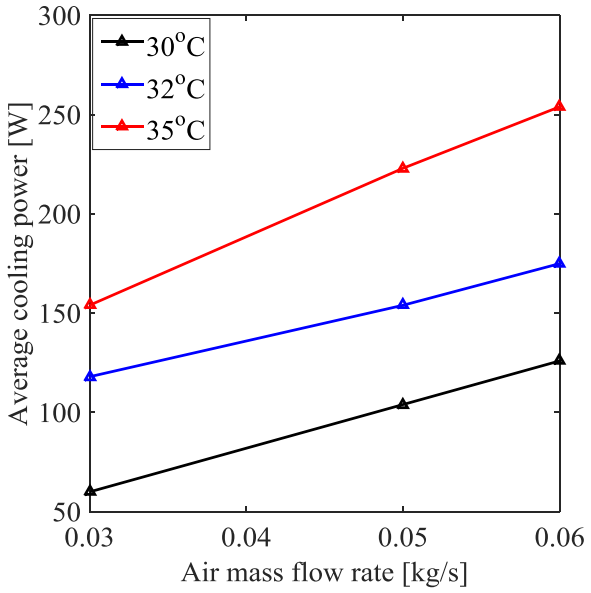

Fig. 10. Effect of air mass flow rate and air inlet temperature on the average cooling power for the RT27 module.

for an air mass flow rate of 0.06 kg/s (thus, a 15% reduction in effectiveness).

From Fig. 8, it can be observed that by increasing the inlet air temperature at a fixed air mass flow rate, does not severely influence the effectiveness. For an inlet air temperature of 30 °C and air mass flow rate of 0.03 kg/s the calculated average effectiveness was 0.60. For an inlet air temperature of 32 °C and air mass flow rate of 0.03 kg/s the calculated average effectiveness was 0.59 (a mere 1.6% reduction in effectiveness) and for an inlet air temperature of 35 °C and airflow rate of 0.03 kg/s the calculated effectiveness was 0.62 (a mere 3.3% increase in effectiveness).

5.5. Average cooling power analysis: effects of the air mass flow rate and the inlet air temperature

Eq. (17) was used to calculate instantaneous cooling power. The instantaneous cooling powers were averaged over the phase transformation duration. The data in Tables 5 and 6 were used to plot the effect of air mass flow rate and air inlet temperature on the average cooling power for the RT25 and RT27 modules as is shown in Figs. 10 and 11.

From Figs. 10 and 11, the effect of the air mass flow rate on cooling power can be observed by considering a fixed average inlet air temperature ($\bar{T}_i$). The effect of the inlet air temperature can be determined likewise by considering a fixed air flow rate. As expected, it is clear from Figs. 10 and 11 that either an increase in the air mass flow rate or an increase in the inlet air temperature increased the average cooling power. The Reynolds number for the air flow in the air channels between plates was calculated to be turbulent (Re = 9697-19 394) over the range of the flow rates tested. For turbulent flow, the higher the air flow rate, the higher the convection heat transfer coefficient. A higher convection heat transfer coefficient increases the convective heat transfer rate from air to PCM. A higher temperature difference between inlet air temperature and PCM melting temperature ($\bar{T}_i - \bar{T}_m$) also increases convection heat transfer rate.

5.6. Phase transformation duration: effect of the air mass flow rate and the inlet air temperature

Figs. 12 and 13 give the phase transformation durations of the PCMs. It can be seen that the durations decreased as either the air flow

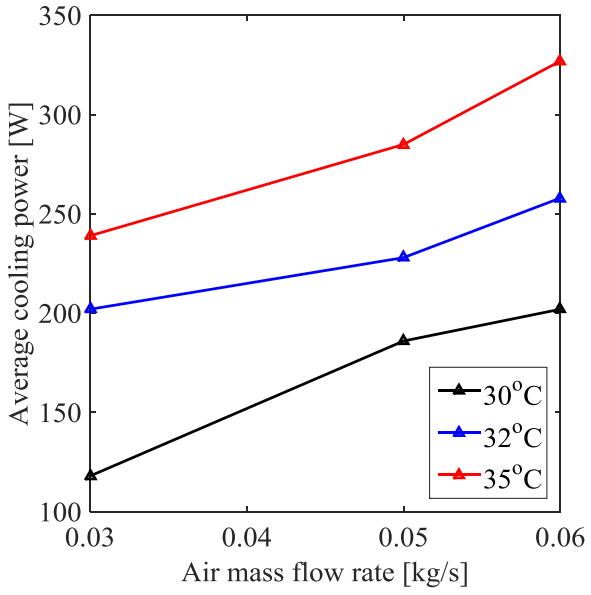

Fig. 11. Effect of air mass flow rate and air inlet temperature on the average cooling power for the RT25 module.

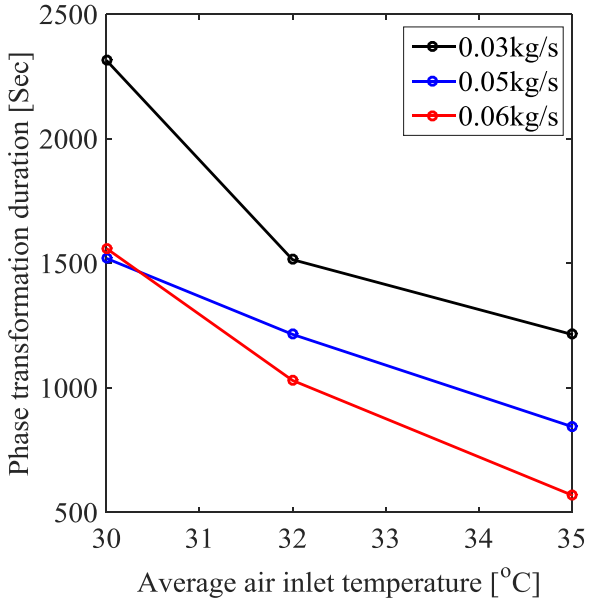

Fig. 12. Effects of the air inlet temperature and the air mass flow rate on the phase transformation duration for the RT25 module.

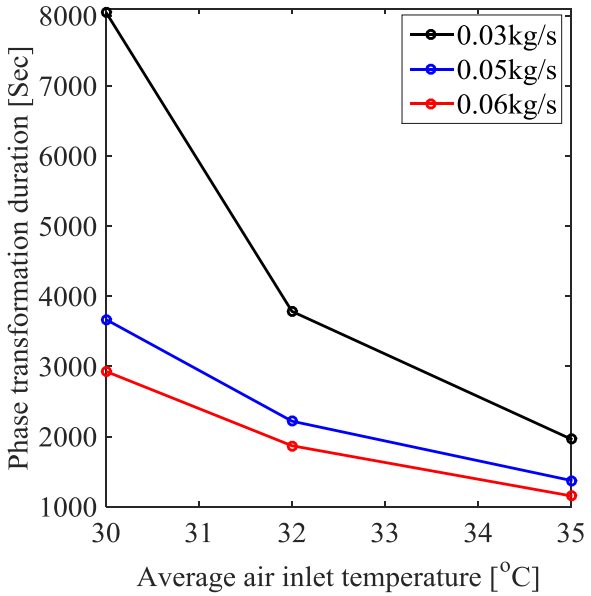

Fig. 13. Effects of the air inlet temperature and the air mass flow rate on the phase transformation duration for the RT27 module.

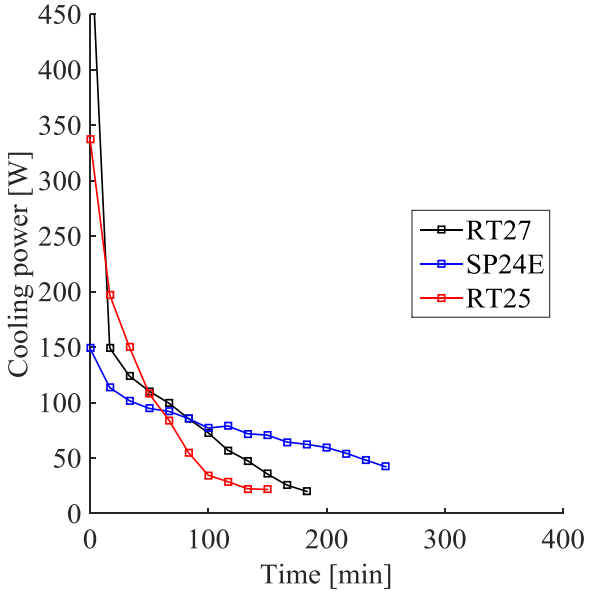

Fig. 14. Comparison of the cooling power delivered by the RT25, RT27 and SP24E modules for an airflow rate of 0.03 kg/s at an air inlet temperature of 32 °C.

rates or the inlet air temperatures increased. For the RT27 module (Fig. 16), for an inlet air temperature of 32 °C and airflow rate of 0.03 kg/s the melting duration was 3785 s. For an inlet air temperature of 32 °C and airflow rate of 0.06 kg/s the melting duration was 1870 s. Doubling the air flow from 0.03 kg/s to 0.06 kg/s reduced the melting duration by 51%. This is attributed to higher heat transfer coefficient for higher air mass flow as will be discussed later.

For the RT27 module (Fig. 13), for an inlet air temperature of 30 °C and airflow rate of 0.03 kg/s the melting duration was 8050 s. For an inlet air temperature of 35 °C and airflow rate of 0.03 kg/s the melting duration was 1965 s; thus, a quarter of the melting duration at 30 °C. This may be attributed to higher heat transfer rates for higher temperature differences between inlet air and PCM melting temperature as will be discussed later.

5.7. Cooling power and cumulative energy absorbed for the entire test period

This section focuses on the results of cooling power and energy absorbed by 15 plates (module) for the entire duration of the experimental test for the three different PCM types (RT27, RT25 and SP24E) and the effects of the airflow rate and the temperature difference between inlet air and PCM melting temperature.

5.8. Comparison of cooling power for three modules

From Fig. 14 it can be seen that the cooling power decayed with time. This was observed for all experimental conditions. The rate of decay was more pronounced for the paraffinic PCMs when compared to the salt hydrate. This can be due to the different mechanisms by which the materials absorb heat; melting for paraffinic PCMs and dehydration

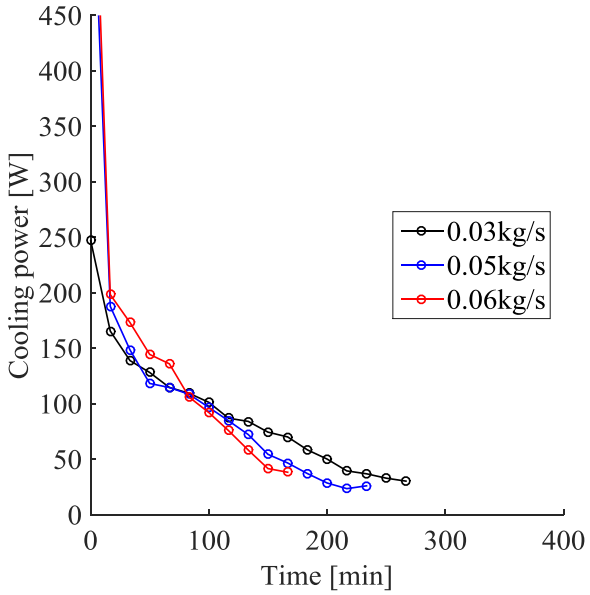

Fig. 15. Effect of the air mass flow rate on the cooling power delivered by the SP24E module at an inlet air temperature of 35 °C.

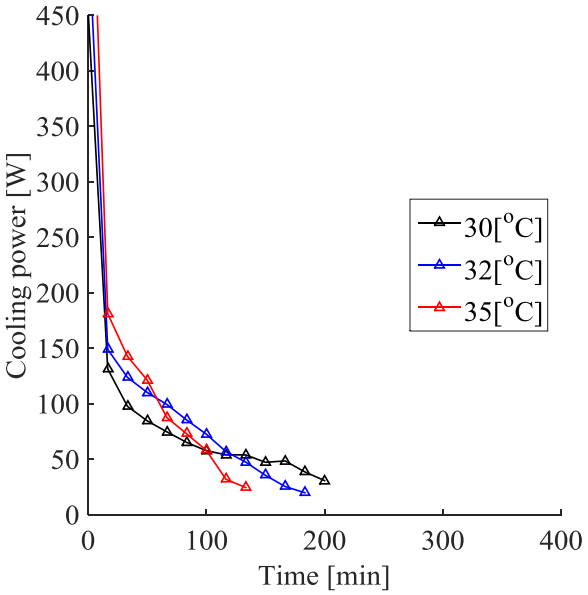

Fig. 16. Effect of inlet air temperature on cooling power delivered by RT27 module at an air mass flow rate of 0.03 kg/s.

for salt hydrate PCMs. SP24E which decayed from 150 W to about 50 W over a period of 250 min, giving an average cooling power decay rate of − 0.4 W/min. The RT27 heat rate decayed from 450 W to 20 W over a period of 180 min, giving an average cooling power decay rate of −2.4 W/min while the RT25 heat rate decayed from 350 W to 20 W over a period of 150 min, giving an average cooling power decay rate of −2.2 W/min.

5.9. Effect of the air mass flow rate on the cooling power

The effect of the air mass flow rate on the cooling power was evaluated by considering a fixed inlet air temperature of 35 °C and varying air mass flow rate for the SP24E module. Fig. 15 indicates that higher cooling power values were achieved at higher air flow rates. Higher air flow rates did, however, also result in short heat absorption time spans. This shows that the melting of the PCM was completed earlier at higher air flow rates. Fig. 15 also shows that for lower airflow rates, the cooling power was lower. However, longer periods of heat absorption could be maintained. The findings as stated above were confirmed for all PCM types and the other air mass flow rates and inlet air temperatures.

5.10. Effect of the air inlet temperature on cooling power

The effect of the inlet air temperature on the cooling power was evaluated by considering a fixed air mass flow rate of 0.03 kg/s and varying inlet air temperature for the RT27 module.

Fig. 16 shows higher values of cooling power for higher inlet air temperature but reaches the minimum value within a short time. This shows that the phase transformation (melting) of the PCM completed earlier at higher inlet air temperature. Fig. 19 also shows that for lower inlet air temperatures, the cooling power was relatively lower. However, the cooling power remained higher than the minimum value for a relatively longer period. The findings as stated above were confirmed for all PCM types and the other air mass flow rates and inlet air temperatures.

5.11. Cumulative energy absorption

Eq. (20) was used to calculate the total energy absorbed for the whole duration of the experiment.

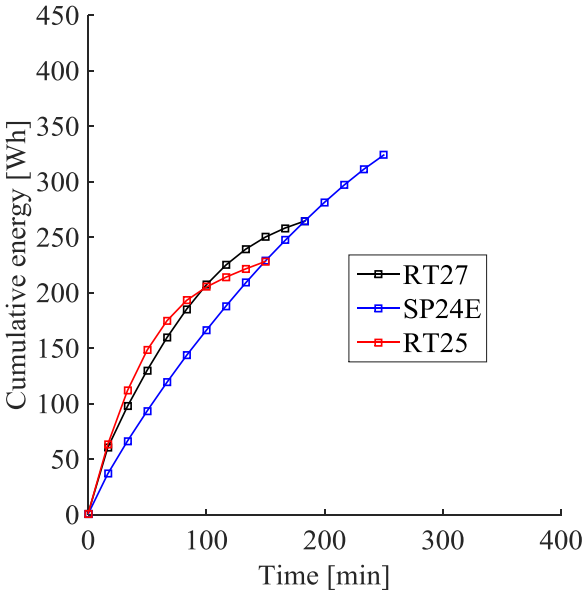

Fig. 17. Comparison of cumulative energy absorption of the RT25, RT27 and SP24E modules for an airflow of 0.03 kg/s and an air inlet temperature of 32 °C.

5.12. Comparison of cumulative energy absorbed for RT25, RT27 and SP24E

A comparison of the energy absorption for RT25, RT27 and SP24E was done by subjecting the three PCMs modules under the same air mass flow rate and approximate inlet air temperature. The comparison is shown in Fig. 17.

From Fig. 17 it can be seen that the SP24E (salt hydrate) module had the highest energy absorption capacity. This was confirmed for all the other air mass flow rates and inlet air temperatures.

This is due to the high overall heat capacity of SP24E (salt hydrates) when compared to the paraffinic PCMs (RT25 and RT27). The specific heat capacities and thicknesses of the RT5, RT27 and SP24E plates were the same, 2 kJ/kg K and 10 mm respectively. The difference between these PCMs is their densities: 880 kg/m^3 for RT25 and RT27 and

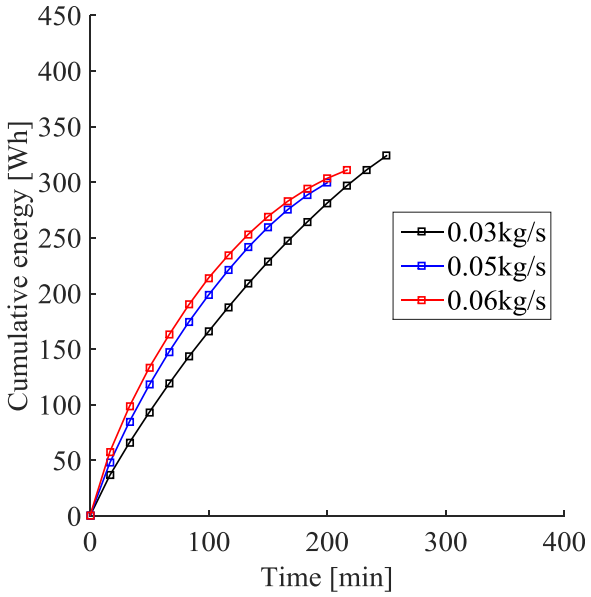

Fig. 18. Effect of air mass flow rate on cumulative energy stored for SP24E module with air inlet temperature of 30 °C.

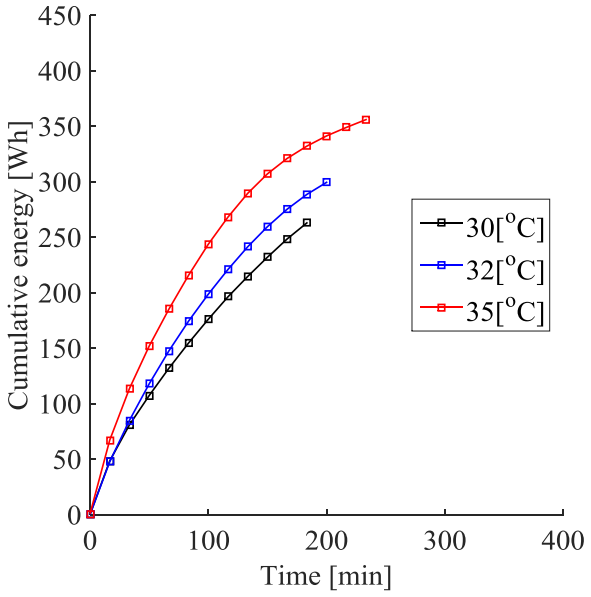

Fig. 19. Effect of inlet air temperature on cumulative energy absorbed into the SP24E module for air mass flow rate of 0.05 kg/s.

1500 kg/m^3 for SP24E. As mentioned, the density of the salt hydrate was almost twice that of paraffin waxes. This means that the salt hydrates overall heat capacity was almost twice that of paraffin waxes for the same volume of encapsulation.

5.13. Effect of the air mass flow rate on the cumulative energy absorption

The effect of the air mass flow rate on the cumulative energy absorbed was evaluated by considering a fixed inlet air temperature of 30 °C and then varying the air flow rate from approximately 0.03 to 0.06 kg/s as is shown in Fig. 18.

From Fig. 18, it was observed that the rate of energy absorption was higher at higher air flow rates. This can be attributed to high convection heat transfer coefficients as is typically expected at high air flow rates. Higher air flow rates result in lower thermal convective resistance on the air side. If the thermal resistance is lower, then more heat is expected to flow from the high temperature region (air) to the lower temperature regions (PCM). Thus, more energy is expected to be absorbed in a given time span. Fig. 18 also shows that more energy was absorbed at lower air mass flow rates when compared to higher air flow rates. This was confirmed for all of the PCM modules for all other inlet air temperature conditions. The expected behaviour was that the total energy absorbed had to be the same regardless of the air mass flow rate for the same PCM initial and final temperatures and experimental duration. The unexpected behaviour may be explained by invoking the incongruent melting of RT27, RT25 and SP24E which were partial or incomplete during the duration of the experiment. It may also be explained by non-uniform inlet air temperatures for the different air mass flow rates.

5.14. Effect of the air inlet temperature on the cumulative energy absorbed

The effect of inlet air temperature on the cumulative energy absorbed can be evaluated by considering a fixed air mass flow rate. In Fig. 19 for instance, the impact of the air temperature for a mass flow rate of 0.05 kg/s is shown for the SP24E module.

From Fig. 19, the rate of energy absorption increased with inlet air temperature. This was confirmed for all of the PCM modules for all other inlet air temperature conditions.

6. Design chart

In order to achieve the second objective of the study, the transient cooling power delivered by 15 plates (one module) was multiplied by integer numbers to obtain the cooling load of more than one module as shown in the design chart Fig. 20. This chart can therefore be used to determine the number of modules that are required to achieve a desired cooling power for a desired time period for the listed air mass flow rate, inlet air temperature, the plate pitch of 15 mm (the pitch that was used in this investigation), and air duct measuring 255 mm by 278 mm (the air duct used in this study). For other sized air ducts, estimation may only be made for air velocities that are the same as in this experimental study.

Using design charts such as this can be a cumbersome task since a different chart has to be generated for specific operating conditions. The design charts also cannot cater for air flow rates in between. They cater only for specific operating conditions tested and for the test conditions that were used in the exact experimental case. Given these limitations in the application of design charts, it can be easily seen that there is need for a better empirical model that will predict the number of modules that will cater for a particular objective cooling load.

7. Empirical model development

In this section the procedure that was followed to develop an empirical model is described. The intention is that it can be used for different air mass flow rates and inlet air conditions. It should be noted that this is only a first order model to determine the type of function that is required to capture the dominant aspects at play.

From Newton's law of cooling, the rate of heat transfer from a fluid in a passage can be expressed as [23]:

$$\dot{Q}_i = h_c A_s \Delta T_{ave} \tag{21}$$

Here h_c is the convective heat transfer coefficient and A_s is the heat transfer surface area for 15 plates.

$$\Delta T_{ave} = T_s - \frac{\bar{T}_i + \bar{T}_o}{2} \tag{22}$$

Here $\frac{\bar{T}_i + \bar{T}_o}{2}$ represents the bulk mean fluid temperature and T_s is the plate surface temperature.

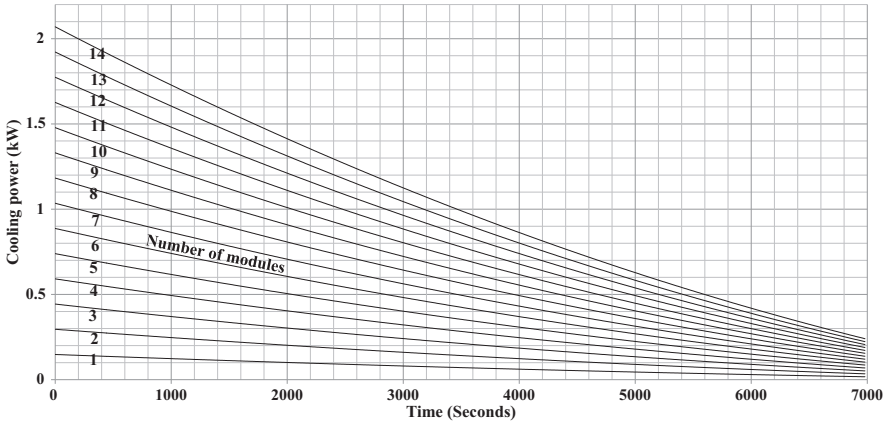

Fig. 20. Design chart for calculating the number of RT25 plates for an air mass flow rate of 0.03 kg/s and inlet air temperature of 30 °C for the experimental test facility located at the Council for Scientific and Industrial Research in Pretoria at an elevation of 1386 m above sea level with barometric pressure of 87.8 kPa.

Table 7
Correlation coefficients, R^2 and RMSE for the different PCM modules.

Correlation coefficients							
Module type	C_0	C_1	C_2	C_3	C_4	R^2	RMSE
RT25	0.293	1.18	1	0.733	− 0.00124	0.94	0.1%
RT27	0.506	0.835	1	0.689	− 0.00108	0.94	0.05%
SP24E	0.115	0.859	1	0.477	− 0.000279	0.94	0.02%

Table 8
Correlation coefficients, R^2 and RMSE for the different PCM modules considering phase transformation only.

Correlation coefficients							
Module type	C_0	C_1	C_2	C_3	C_4	R^2	RMSE
RT25	0.223	0.981	1	0.6	− 0.000898	0.98	0.02%
RT27	0.352	0.748	1	0.627	− 0.000851	0.98	0.01%

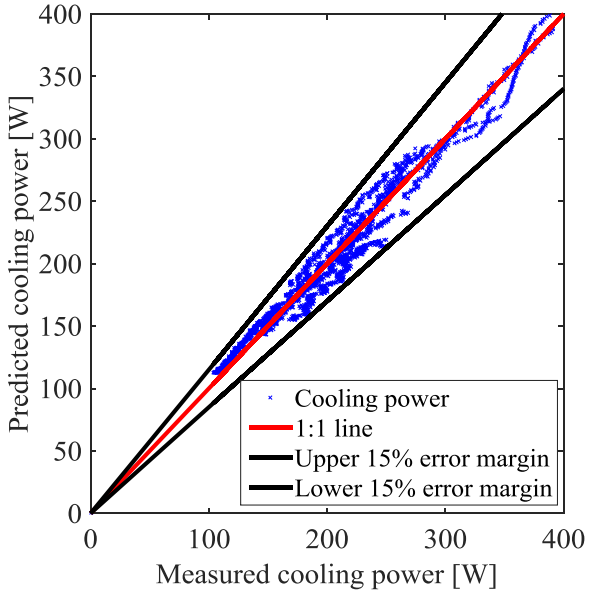

Fig. 21. Predicted cooling power versus the measured cooling power for RT25.

The thermal resistance of the aluminium encapsulation is very small and therefore it was ignored and the PCM temperature can be assumed to be equal to the plate surface temperature.

The PCM-test section was well insulated and the heat losses to the surroundings were in the range of 0.4–2.3 W. For the purpose of simplifying the derivation of the heat transfer rate to the PCM using Eq. (21), these heat losses were ignored. Substituting for ΔT_{ave}, Eq. (21) becomes

$$\dot{Q}_i = hA_s\left(T_s - \frac{\overline{T}_i + \overline{T}_o}{2}\right) \tag{23}$$

Considering the energy balance of air between the inlet and outlet of the PCM-air heat exchanger,

$$\dot{Q}_i = hA_s\left(T_s - \frac{\overline{T}_i + \overline{T}_o}{2}\right) = \dot{m}C_p(\overline{T}_o - \overline{T}_i) \tag{24}$$

Now $T_s - \overline{T}_i = \Delta T_{pcm}$

$$\dot{Q}_i = \frac{hA_s\,\Delta T_{pcm}}{\left(1+\frac{hA_s}{2\dot{m}C_p}\right)} \tag{25}$$

Eq. (25) was derived for steady state conditions and may not be strictly applicable for transient conditions where the cooling power decreases with time.

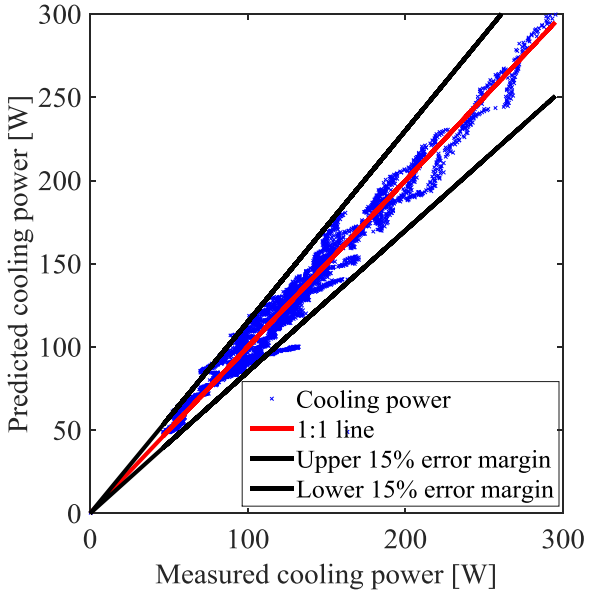

Fig. 22. Predicted cooling power versus the measured cooling power for RT27.

7.1. Correlation analysis

From the derived steady state Eq. (25), it is clear that the cooling

power of the heat exchanger is influenced by air flow rate ($\dot{m}$) and the difference between inlet and PCM melting temperatures (ΔT_{pcm}), heat transfer surface area (A_s) and specific heat capacity of heat transfer fluid. Different empirical functions were analysed using Eureka curve fitting Software version 1.24.0 developed by Nutonian incorporation. The data points i.e. PCM instantaneous cooling power ($\dot{Q}_i$), air mass flow rate ($\dot{m}$), difference between inlet and PCM melting temperatures (ΔT_{pcm}) and time (t) for each PCM module were loaded into Eureka and different functions were tested to check their suitability for the correlation of the data points. Heat transfer surface area (A_s) and specific heat capacity of heat transfer fluid were kept constant. Eureka predictions showed that the general function representing the relationship is an exponential function of the form:

$$\dot{Q}_i = C_0 \Delta T_{pcm}{}^{C1} C_2 \dot{m}^{C3} e^{(-C4t\Delta T_{pcm}\dot{m})} \quad (26)$$

7.2. Comparison of measured and predicted cooling power for PCM modules for entire experimental test period

A large number of data points ($\dot{Q}_i$, ΔT_{pcm}, $\dot{m}$ and t) for each of the PCMs were substituted into Eq. (26). For SP24E PCM 26,567 data points were used, for RT27 14,667 data points were used and for RT25 12,468 data points were used. Predicted functions for each of the PCMs modules, correlation coefficients and the root mean square errors for the 3 PCM modules are shown in Table 7.

7.3. Comparison of measured and predicted cooling power for PCM modules during phase transformation period

For the paraffinic PCMs RT25 and RT27 definite phase transformation duration was determined as explained earlier. The data points ($\dot{Q}_i$, ΔT_{pcm}, $\dot{m}$ and t) for the RT25 and RT27 modules for the phase transformation only were substituted again into Eq. (26): 2377 data points for the RT25 module and 5409 data points for the RT27 module. Correlation coefficients, R^2 and RMSE for the different PCM modules considering phase transformation only are shown in Table 8.

The goodness of fit (R^2) of the model in Table 8 was higher than that obtained when considering the entire experimental test range (See Table 7). The reason for the higher R^2 values was that the model more accurately predicted the cooling power within the phase transformation period.

Figures 24 and 25 show a comparison of real measured cooling power ($\dot{Q}_i$) values predicted by the empirical models for RT5 and RT27 modules for the phase transformation period only. The red line in Figs. 21 and 22 represents the exact correlating line. The black lines represent a deviation of ± 15% from the experimental data.

7.4. Application of equations to design

Given a desired objective cooling load, inlet air temperature, air mass flow rate and time, the number of modules, n, installed in parallel is given by Eq. (27).

$$n_{mod} = \frac{\dot{Q}_{obj}}{C_0 \Delta T_{pcm}{}^{C1} C_2 \dot{m}^{C3} e^{(-C4t\Delta T_{pcm}\dot{m})}} \quad (27)$$

In order to maintain the desired objective cooling load (Q_{obj}), a safety factor of 15% should be applied to the calculated number of modules as the maximum permissible error for RT25 and RT27 modules as shown in Figs. 21 and 22 was 15%. Note that the correlation is only valid for the test geometries considered in this investigation in terms of plate pitch and air velocity.

8. Conclusions

The purpose of this study was to experimentally evaluate and compare the cooling performance of three PCM materials in plate-air heat exchanger modules subjected to Southern African climatic conditions and to use the data to deduce empirical correlations that can be used by thermal designers to determine the number of modules required to maintain an objective cooling load within the range of operating conditions.

- Based on the experimental results, the following conclusions were derived: All the three types of PCMs (RT27, RT25 (paraffin type) and SP24E (salt hydrate type)) investigated in this study exhibited air cooling behaviour, therefore they can be applied for building free cooling applications under Southern African climatic conditions. However a huge number of the PCM plates are required to offset a mere portion of the cooling load.
- It was found that paraffinic PCMs exhibited high instantaneous heat absorption with short heat absorption duration. Salt hydrate exhibited longer heat absorption duration but had a lower instantaneous heat absorption capacity than the paraffin.
- The salt hydrate (SP4E) module had the highest energy absorption capacity for all experimental conditions.
- A new empirical model with different coefficients for different PCMs was successfully developed. The model can be used for determining the number of modules installed in parallel with a plate pitch of 15 mm with a mass flux i.e air mass flow rate per module divided by the cross sectional area of each module in the range of 0.42 kg/m^{2}s to 0.85 kg/m^{2}s and inlet air temperatures ranging from 30 °C to 35 °C to maintain an objective cooling load for a desired time period.

References

[1] A. Waqas, Z.U. Din, Phase change material (PCM) storage for free cooling of buildings – a review, Renew. Sustain Energy Rev. 18 (2013) 607–625.
[2] E. Osterman, V.V. Tyagi, V. Butala, et al., Review of PCM based cooling technologies for buildings, Energy Build. 49 (2012) 37–49.
[3] South Africa Department of Environmental Affairs. National climate change response: White paper. Pretoria, South Africa.
[4] V.A. Raj, R. Velraj, Heat transfer and pressure drop studies on a PCM-heat exchanger module for free cooling applications, Int. J. Therm. Sci. 50 (2011) 1573–1582.
[5] J.R. Turnpenny, D.W. Etheridge, D.A. Reay, Novel ventilation cooling system for reducing air conditioning in buildings. Part I: testing and theoretical modelling, Appl. Therm. Eng. 20 (2000) 1019–1037.
[6] K. Yanbing, J. Yi, Z. Yinping, Modeling and experimental study on an innovative passive cooling system — NVP system, Energy Build. 35 (2003) 417–425.
[7] M. Alam, J. Sanjayan, P.X.W. Zou, et al., Evaluating the passive and free cooling application methods of phase change materials in residential buildings: a comparative study, Energy Build. 148 (2017) 238–256, https://doi.org/10.1016/j.enbuild.2017.05.018.
[8] S. Medved, C. Arkar, Correlation between the local climate and the free-cooling potential of latent heat storage, Energy Build. 40 (2008) 429–437.
[9] A. Lazaro, P. Dolado, J.M. Marín, B. Zalba, PCM – air heat exchangers for free-cooling applications in buildings: experimental results of two real-scale prototypes, Energy Convers. Manag. 50 (2009) 439–443.
[10] N. Chaiyat, T. Kiatsiriroat, Energy reduction of building air-conditioner with phase change material in Thailand: case study, Therm. Eng. 4 (2014) 175–186.
[11] E. Halawa, W. Saman, Thermal performance analysis of a phase change thermal storage unit for space heating, Renew. Energy 36 (2011) 259–264.
[12] M.J. Kabbara, N. Ben Abdallah, Experimental investigation on phase change material based thermal energy storage unit, Procedia - Procedia Comput. Sci. 19 (2013) 694–701.
[13] M. Rajagopal, R. Velraj, Experimental investigation on the phase change material-based modular heat exchanger for thermal management of a building, Int. J. Green. Energy 13 (2016) 1109–1119.
[14] A. Castell, M. Belusko, F. Bruno, L.F. Cabeza, Maximisation of heat transfer in a coil in tank PCM cold storage system, Appl. Energy 88 (2011) 4120–4127.
[15] N.H.S. Tay, M. Belusko, F. Bruno, Experimental investigation of tubes in a phase change thermal energy storage system, Appl. Energy 90 (2012) 288–297.
[16] Onset Indoor HOBO H8 family. Onset, Bourne, Massachusetts
[17] ASHRAE ASHRAE Standard 94.1: Method of testing active latent-heat storage devices based on thermal performance. Georgia Atlanta, 2010.
[18] P. Dolado, A. Lazaro, J.M. Marin, B. Zalba, Characterization of melting and solidification in a real scale PCM-air heat exchanger: numerical model and experimental validation, Energy Convers. Manag. 52 (2011) 1890–1907.
[19] M.M. Farid, A.M. Khudhair, S. Ali, K. Razack, A review on phase change energy storage: materials and applications, Energy Convers. Manag. 45 (2004) 1597–1615.
[20] Rubitherm, Rubitherm website.pdf. 〈https://www.rubitherm.eu/index.php/

produktkategorie/makroverkaspelung-csm〉. (Accessed 27 October 2017), 2017.
[21] Rubitherm Phase Change Material Safety data sheet SP24E. 〈https://www.rubitherm.eu/index.php/produktkategorie/anorganische-pcm-sp〉. (Accessed 7 Dec 2017).
[22] Statistics South Africa Building statistics, 2014. Pretoria, South Africa, 2016.
[23] Y.A. Cengel, Heat Transfer: A Practical Approach, Second., McGraw-Hill, New York, 2008.
[24] Z.K. Morvay, D.D. Gvozdenac Toolbox 6 Thermodynamic and transport properties of moist air. Appl. Ind. energy Environ. Manag. part III Fundam. Anal. Calc. energy Environ. perfomance.
[25] ASHRAE Psychrometrics. ASHRAE Fundam. Handb. SI, 2002.
[26] Corp RI The Rotronic Humidity Handbook. Rotronic Instrument Corp., New York, 2005.
[27] R.J. Moffat, Describing the uncertainties in experimental results, Exp. Therm. Fluid Sci. 1 (1988) 3–17.
[28] J.P. Holman, Experimental Methods for Engineers, Eighth, McGraw-Hill, New York, USA, 2012.